THE JOURNAL OF PHYSICAL CHEMISTRY LETTERS
A JOURNAL OF THE AMERICAN CHEMICAL SOCIETY

pubs.acs.org/JPCL Letter

Chemical and Structural In-Situ Characterization of Model Electrocatalysts by Combined Infrared Spectroscopy and Surface X-ray Diffraction

Olaf Brummel,* Leon Jacobse, Alexander Simanenko, Xin Deng, Simon Geile, Olof Gutowski, Vedran Vonk, Yaroslava Lykhach, Andreas Stierle, and Jörg Libuda

Cite This: https://doi.org/10.1021/acs.jpclett.3c01777 Read Online

ACCESS | Metrics & More | Article Recommendations | Supporting Information

ABSTRACT: New diagnostic approaches are needed to drive progress in the field of electrocatalysis and address the challenges of developing electrocatalytic materials with superior activity, selectivity, and stability. To this end, we developed a versatile experimental setup that combines two complementary in-situ techniques for the simultaneous chemical and structural analysis of planar electrodes under electrochemical conditions: high-energy surface X-ray diffraction (HE-SXRD) and infrared reflection absorption spectroscopy (IRRAS). We tested the potential of the experimental setup by performing a model study in which we studied the oxidation of preadsorbed CO on a Pt(111) surface as well as the oxidation of the Pt(111) electrode itself. In a single experiment, we were able to identify the adsorbates, their potential dependent adsorption geometries, the effect of the adsorbates on the surface morphology, and the structural evolution of Pt(111) during surface electro-oxidation. In a broader perspective, the combined setup has a high application potential in the field of energy conversion and storage.

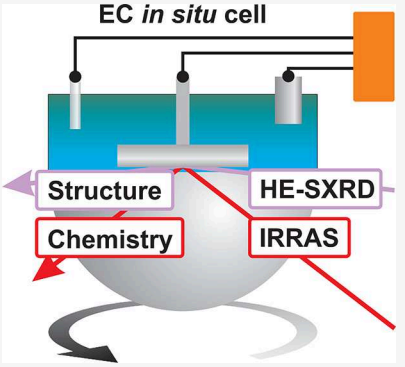

Electrocatalysis is at the heart of a future energy system based on renewable resources.[1−8] Typically, the most active electrocatalysts retain a high level of complexity in terms of both structure and chemical composition.[8−10] The electrocatalytic properties of such systems are dynamic under operation conditions as a result of processes such as dealloying, sintering, surface segregation, dissolution, bulk diffusion, surface oxidation, and phase transformations.[11−15] In most cases, activity, selectivity, stability, and structural dynamics are controlled by the interfacial chemistry at the electrified interface associated with specific adsorption processes, the formation of surface intermediates, coadsorption of poisons or promoters, formation of hydroxyls and hydroxides, and the formation and desorption of products.[16−19] Under these conditions, surface structure and surface chemistry become intimately entangled, in both a static and dynamic picture. To understand structure−activity relationships in electrocatalysis, it is therefore essential to study surface structure and surface chemistry in a correlated manner. In the past decades, a wide range of characterization techniques coupled with in-situ electrochemical cells have been developed to provide detailed insights into the structural (X-ray diffraction,[20] scanning probe microscopy,[21−24] electron and photon-based microscopy[25−27]) and chemical properties (infrared spectroscopy,[28−32] sum-frequency spectroscopy,[33] photoelectron spectroscopy,[34,35] X-ray absorption spectroscopy[36]) of electrocatalytic interfaces. However, in almost all cases, these experiments are performed separately in different environments and on different samples, making it intrinsically difficult to correlate complementary information. The potential of combining structural and chemical information in electrocatalysis has been demonstrated, for example, by studies by Villegas and Weaver[37] as well as by Marković et al.,[38] which have contributed significantly to our current understanding of the CO oxidation on Pt(111). However, these studies are also subject to the uncertainty that structural and chemical information was obtained in separate experiments. This problem could be overcome if the experimental information was recorded simultaneously on the same sample. Examples from heterogeneous catalysis demonstrate the potential of such multimethod approaches.[39−44] To this end, we developed a unique electrochemical in-situ setup that combines high energy surface X-ray diffraction (HE-SXRD) and infrared reflection absorption spectroscopy (IRRAS). Both techniques can be used simultaneously under electrochemical conditions, making use of the high penetration of high-energy X-rays through

Received: June 29, 2023
Accepted: September 15, 2023

https://doi.org/10.1021/acs.jpclett.3c01777
J. Phys. Chem. Lett. XXXX, XXX, XXX−XXX

IRRAS optics. In a unique way, this versatile setup allows us to obtain combined information about the interface structure and interface chemistry during the electrocatalytic reaction. Potentially, instrumentation can be used to advance the fundamental understanding of electrode materials in emerging technologies for energy conversion and storage.

In the present paper, we provide a detailed description of this versatile setup and demonstrate its huge potential using a simple model reaction. We scrutinize the stepwise oxidation of adsorbed CO on a Pt(111) electrode and the surface oxidation of the electrode itself. The concept of the setup is illustrated in Figure 1. In principle, both HE-SXRD and IRRAS are

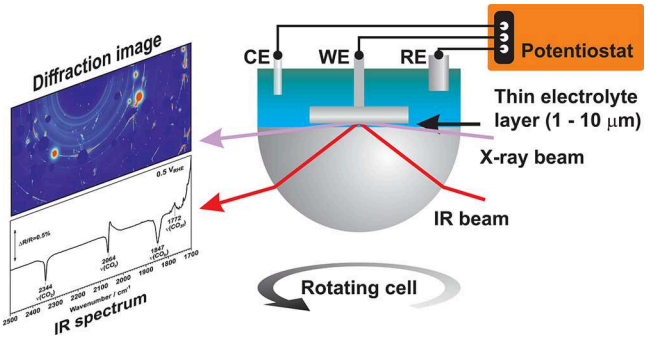

Figure 1. Concept of the combined setup for simultaneous structural and chemical analysis by means of electrochemical HE-SXRD and IRRAS methods.

performed simultaneously in an electrochemical cell, which is compatible with both methods. Specifically, the cell is based on a three-electrode configuration. A planar model electrode, e.g., a single crystal or nanoparticles on a planar support,[45] serves as the working electrode (WE). The latter is fully immersed into the electrolyte and gently pressed against the CaF_2 window to ensure a constant thickness of the thin layer of electrolyte (typically ~1−10 μm) between the window and the sample during the measurement.[32]

IR light enters through an IR-transparent focusing window (CaF_2 or ZnSe). The high-energy X-ray beam enters directly through the cell walls made of low absorption materials PEEK and Kalrez. The diffracted beam passes through the CaF_2 window with 12.5 mm radius (X-ray absorption of 70% at photon energy of 73.74 keV).[46] The setup allows us to image a large part of reciprocal space with a 2D detector and high-energy X-rays.[47] Different azimuthal planes can be sampled due to the rotation mechanism of the cell. Small scattering angles below 10° ensure geometric compatibility with the EC-IRRAS setup.

The schematic representation of the setup is shown in Figure 2. The setup consists of a Fourier-transform infrared (FTIR) spectrometer with evacuated optics (Bruker Vertex 80v) with modular customized detector boxes for conventional EC-IRRAS and polarization modulation (PM) EC-IRRAS (both inert gas purged) on an adjustable optical table. The height and tilt of the optical table can be adjusted by three z-stages with high-precision worm gear drives (Huber Diffraktionstechnik). The spectrometer features both static polarization and polarization modulation, depending on the application requirements.

The EC-IRRAS module is equipped with an external IR chamber fixed at the spectrometer. The chamber houses the electrochemical cell mounted on a rotating aluminum arm

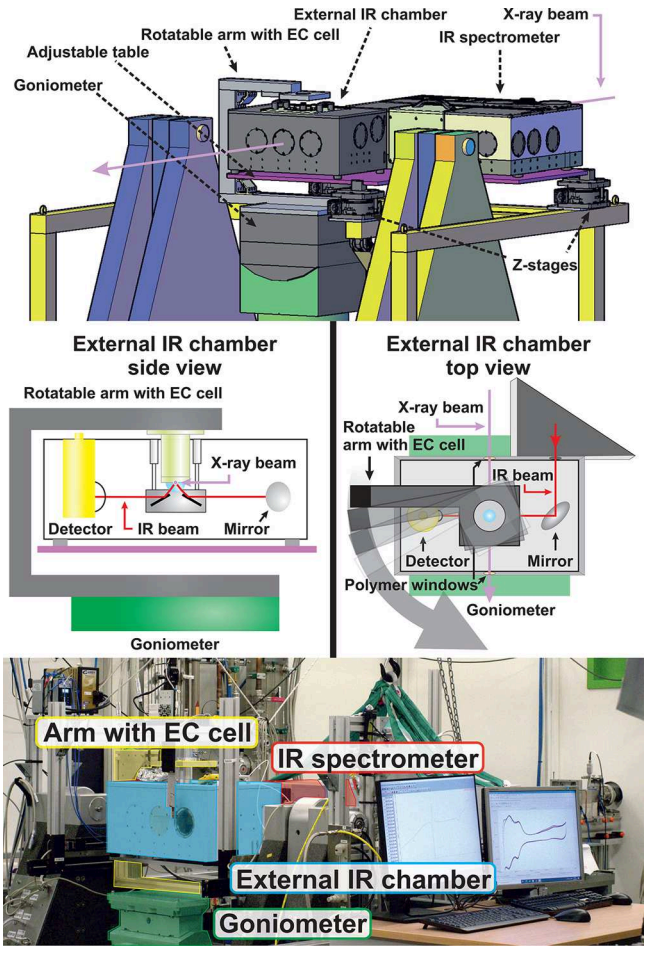

Figure 2. Schematic representation of the setup (top panel) with a detailed side and top view of the electrochemical cell with a rotation mechanism (middle panel). The photography of the setup (bottom panel) was taken in the hutch of the beamline P07 at PETRA III, DESY.

(Figure 2, top panel). The detailed view of the external IR chamber is shown in the middle panel of Figure 2 from both side and top perspectives. The arm holding the cell is attached to the goniometer, which allows rotation of the cell together with the sample by an angle of 110° without blocking the optical path of the X-rays. Inside the external IR chamber, the optical paths of the IR and X-ray beams are superimposed at the surface of the sample. The reflected IR light is measured by a liquid nitrogen cooled mercury cadmium telluride (MCT) narrow-band mid-IR detector (Bruker) inside the external IR chamber. The X-rays pass through two polymer windows (PEEK or Kapton) before they reach the 2D detector, which allows purging the chambers with N_2.

To demonstrate the potential of the setup, we performed a model experiment involving the electrochemical oxidation of an adsorbate (CO_{ads}) and the electrode itself (Pt(111)) in an aqueous electrolyte (0.1 M $HClO_4$). The experiment was performed at second experimental hutch (EH2) at beamline P07 at the PETRA III light source at the Deutsches Elektronen Synchrotron (DESY) (Hamburg, Germany).[48] A photograph of the experimental setup at beamline P07 is shown in Figure 2, bottom panel. The experimental procedure is shown in Figure 3a. First, the electrolyte was purged with Ar for 10 min and then with CO for 10 min while the Pt(111) was kept at

https://doi.org/10.1021/acs.jpclett.3c01777
J. Phys. Chem. Lett. XXXX, XXX, XXX−XXX

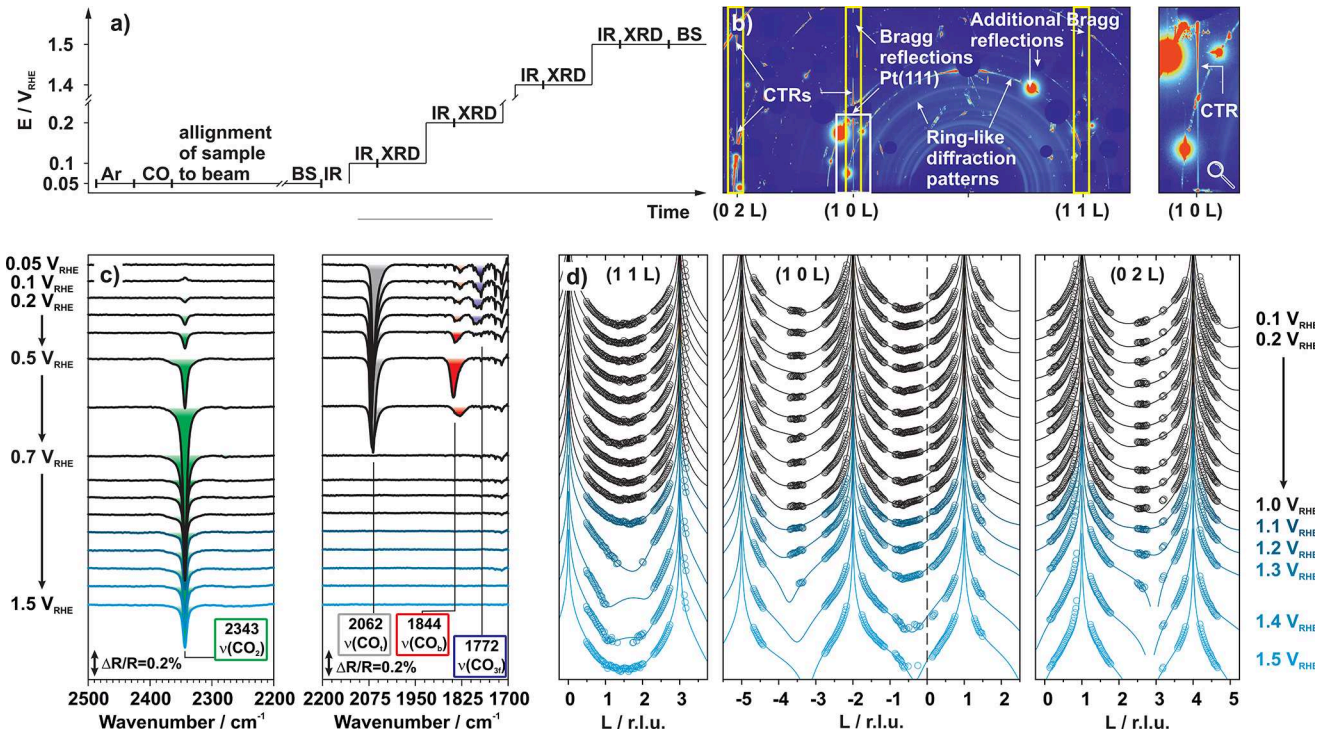

Figure 3. Stepwise oxidation of CO and Pt(111) monitored in the combined HE-SXRD and IRRAS experiment: (a) experimental procedure; (b) representative diffraction pattern (at 0.2 V_{RHE}); (c) potential-dependent IRRA spectra; background IRRA spectra are acquired for the region of CO_2 (left) at 0.05 V_{RHE} before the measurement and for CO_{ads} (right) at 1.5 V_{RHE} after the measurement; (d) corresponding (11), (10), (01), and (02) CTR data (symbols) and fits (solid lines). Note that the (01) CTR is shown as (1 0 $-L$). Data in (c) and (d) are vertically offset for clarity.

0.05 V_{RHE}. The potential was then increased in steps of 0.1−1.5 V_{RHE}. At each potential, we recorded both the IR spectra and the SXRD patterns. The typical example of a diffraction pattern obtained from Pt(111) at 0.2 V_{RHE} is shown in Figure 3b. We observed Bragg reflections from Pt(111) and Bragg reflections and ring-like diffraction patterns from the CaF_2, PEEK, and Kalrez parts of the cell. The most intense Bragg reflections are shielded with beam stops, which can be seen as rectangular, square, and round impressions. For the analysis of the surface structure and morphology of the Pt(111) electrode, we focus our attention on the crystal truncation rods (CTRs), which appear as vertical streaks indicated by rectangular yellow boxes in Figure 3b. Figures 3c and 3d show the potential-dependent IRRA spectra and the corresponding structure factors of the (11), (10), (01), and (02) CTRs between 0.05 and 1.5 V_{RHE}, respectively. Note that the IRRA spectra (Figure 3c) are differential spectra. To reference against clean backgrounds, we separated the spectra into two frequency regions. Between 1700 and 2200 cm^{-1} we expect bands of adsorbed CO_{ads}. In this spectral region, we referenced the spectra against a background spectrum measured after the experiment at 1.5 V_{RHE}, where all CO_{ads} is oxidized to CO_2.[49] Between 2200 and 2500 cm^{-1} we expect bands from CO_2 which are formed during the reaction. Here we used the background spectrum before the measurement at a potential of 0.05 V_{RHE}, which is below the onset of CO oxidation and provides a clean background without product.[49] Between 0.05 and 0.3 V_{RHE}, we observe sharp bands at 2062, 1844, and 1772 cm^{-1}, corresponding to CO adsorbed in on top (CO_t), bridge bonded (CO_b), and 3-fold (CO_{3f}) geometry, respectively.[37] With SXRD we could not detect any specific adlayer structure. For CO-saturated solutions, it is reported that CO adsorbs at 0.05 V_{RHE} in a (2 × 2) CO adlayer in which CO_t and CO_{3f} are present.[37] Magnussen et al. report a dynamically fluctuating (1 × 1) CO layer,[50,51] during the transition from the (2 × 2) to the $(\sqrt{19} \times \sqrt{19})$ CO adlayer. This structure exhibits only short-range order, and its high mobility might result in occupation of both 3-fold and bridging adsorption sites.[51] We attribute the presence of additional CO_b to a slightly lower CO coverage resulting in the mobile (1 × 1) adlayer structure. The lower CO coverage we assign to the long waiting times during the alignment, during which we could not purge with CO for technical reasons. Note that the time scale of diffusion between the thin layer and the bulk solution is on the order of hours (see the Supporting Information). The shape of the CO_t band indicates a defect-lean surface, as low-coordinated adsorption sites would give rise to a very characteristic shoulder at lower wavenumbers.[52] The structure factors of the (11), (10), (01), and (02) CTRs measured in this potential region are consistent with ordered Pt(111) structure.[53] With increasing potential, the IR bands of the CO_{ads} shift to higher wavenumbers, which can be attributed to the Stark effect. For the most intense and sharp CO_t band, we observe a Stark slope of 21 cm^{-1} V^{-1} (Figure S1), which is in good agreement with literature.[32] At 0.5 V_{RHE}, the IR band at 1847 cm^{-1} assigned to CO_b increases in intensity by a factor of ∼5, while the band at 1773 cm^{-1} assigned to CO_{3f} disappears. At the same time, a new band at 2343 cm^{-1} appears, corresponding to the formation of CO_2. These observations indicate the onset of CO oxidation and the transition to the $(\sqrt{19} \times \sqrt{19})$ CO adlayer.[37] Note that we could not detect the $(\sqrt{19} \times \sqrt{19})$ CO adlayer in the HE-SXRD data. However, this is in agreement with previous work by Marković et al.[38] They explain this phenomenon with a missing long-range order of the $(\sqrt{19} \times \sqrt{19})$ CO adlayer. At 0.7 V_{RHE}, no bands assigned to CO_{ads} are observed, and the intensity of the band at 2343

https://doi.org/10.1021/acs.jpclett.3c01777
J. Phys. Chem. Lett. XXXX, XXX, XXX−XXX

cm^{-1}, corresponding to CO_2, reaches its maximum, while the intensity decreases with increasing time. These observations indicate that CO is completely oxidized to CO_2. The latter is first present in solution but, then, slowly diffuses out of the thin layer. The CO oxidation process results in small changes of the CTR intensity profiles discussed further below. As the potential is increased above 1.0 V_{RHE}, the CTR profiles change more drastically, which can be attributed to the onset of Pt oxidation. It is generally accepted that the oxidation of Pt(111) occurs via a place-exchange (PE) mechanism.[54−58] In the PE process (Figure S5), Pt surface atoms are vertically displaced from the surface by approximately a single Pt(111) step height. Note that as described previously, we additionally expect the formation of poorly ordered oxide that is not epitaxially aligned with the underlying Pt metal lattice and cannot be detected in the diffraction experiment.[58,59]

To obtain a more detailed picture, we further analyzed the potential-dependent IRRA spectra and HE-SXRD data. Specifically, we determined the band intensities of the IRRA spectra and fitted the HE-SXRD data to a model describing the PE process. The CTRs are sensitive to only layers ordered with the same periodicity as the Pt(111) crystal structure. Therefore, the Pt atoms that are removed from the substrate to form the poorly ordered oxide do not contribute to the CTRs. As a result, the PE model, which we use to fit the data, is not mass-conserving and thus implies a number of "missing" Pt atoms, which are assumed to be part of the oxide because Pt dissolution in the electrolyte is negligible.[60] Oxygen atoms (possibly occupying the vacancies formed in the subsurface) are not included in the model because their scattering intensity is negligible as compared to that of Pt.[58] Vertical displacements and isotropic Debye−Waller factors are fitted for three atomic layers, i.e., the place-exchange layer (Pt_{PE}), the topmost surface layer (Pt_{sur}), and the underlying base layer (Pt_{base}). The occupancy of the Pt_{base} layer is fixed at unity, and it is fitted for the Pt_{PE} and Pt_{sur} layers. Including an overall scale factor, this results in a total of 9 fit parameters. Simulations (see the Supporting Information) and literature[61] indicate that the scattering strength of the CO molecules themselves is not significant, and therefore they are omitted from the model (similar as for the O atoms). Thus, the intensity of the CTRs is completely dominated by Pt scattering. However, if the adsorption of CO leads to a significant displacement of the Pt_{sur} layer, this should be visible in the data and should also be captured by the fits.[61] For consistency, the same model was used for the entire potential window.

In Figure 4, we have plotted the evolution of the band intensities of the CO_{ads} and CO_2 bands determined from the IRRA spectra (Figure 4a), the total Pt occupancy (Pt_{sur} + Pt_{PE}), the occupancy of Pt_{sur} and Pt_{PE} (Figure 4b), and the corresponding z-positions of Pt_{PE}, Pt_{sur}, and Pt_{base} determined from the HE-SXRD data as a function of the potential (Figure 4c). Note that we provide an overview of all fit parameters in Chapter 3 of the Supporting Information. At 0.05 and 0.1 V_{RHE}, we observe the bands of CO_t, CO_b, and CO_{3f}. Note that a direct correlation between the band intensity in IRRA spectra and coverage is not possible due to coupling effects and different dynamic dipoles moments.[37] For example, the CO_t gives rise to a much more intense band than CO_b and CO_{3f}.[37] Therefore, we discuss the IRRA data only qualitatively.

In the SXRD data, we observe a positive displacement of the Pt_{sur} layer of ~0.05 Å, while in the absence of CO (between 0.7 and 1.0 V_{RHE}) no displacement is observable. Previous work has reported an expansion of 0.09 ± 0.02 Å in the presence of adsorbed CO.[61] We attribute the deviation to the lower CO coverage, as suggested by IR spectroscopy. Between 0.05 and 0.4 V_{RHE}, the initial intensity ratio between CO_t, CO_b, and CO_{3f} changes only slightly, and we observe traces of CO_2 formation. We attribute these changes to the CO oxidation at defect sites. At 0.5 V_{RHE} we observe an increase in CO_2 formation, a decrease in the intensity of the CO_{3f} band at 1773 cm^{-1}, and an increase in the intensity of the CO_b band at 1847 cm^{-1}. These observations indicate the transition to the $(\sqrt{19} \times \sqrt{19})$ CO adlayer,[37] as discussed above. Interestingly, this transition is accompanied by a relaxation of the positive displacement of the Pt_{sur} layer. This demonstrates that the lattice expansion in the presence of CO is strongly dependent on the nature of the CO adlayer. The formation of CO_2 reaches a maximum at 0.6 V_{RHE} and at 0.7 V_{RHE} all CO is oxidized. CTR fits show no displacements in the potential range between CO oxidation at 0.7 and 1.0 V_{RHE}, except for some occupancy of the place exchange site atoms. In this potential region, the surface structure is close to a bulk terminated Pt(111) surface. The nonzero value for the occupancy of the Pt_{PE} over the entire potential range is an indication of residual surface roughness. Only at the onset of oxidation do we expect an increased occupation of this layer. This effect is indeed observed at potentials ≥1.0 V_{RHE}. Simultaneously, the Pt_{sur} occupancy and the total occupancy (Pt_{PE} + Pt_{sur}) decrease, indicating that a poorly ordered oxide is formed at the surface.[58] In the potential region of the Pt

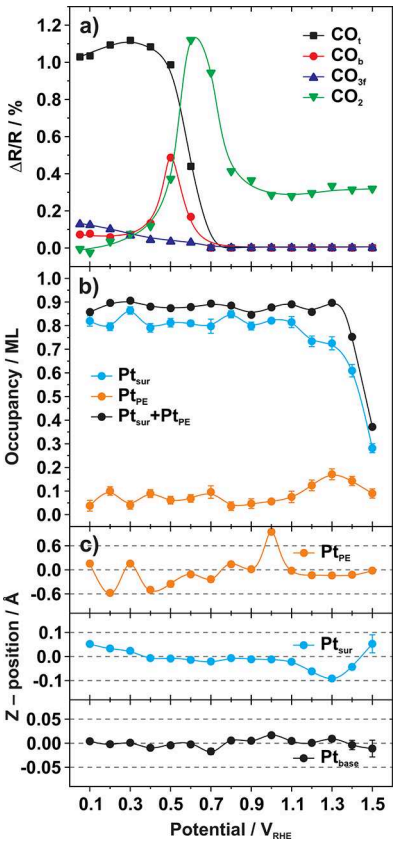

Figure 4. Potential-dependent evolution of adsorbates and surface: (a) intensities of the CO_{ads} and CO_2 bands determined from the IRRA spectra, (b) Pt occupancy, and (c) corresponding z-positions determined from the HE-SXRD data.

https://doi.org/10.1021/acs.jpclett.3c01777
J. Phys. Chem. Lett. XXXX, XXX, XXX−XXX

oxidation, no changes in the IR signals are observed, indicating the absence of molecular adsorbates.

In summary, we developed a new experimental setup which combines in-situ high-energy surface X-ray diffraction (HE-SXRD) and infrared reflection absorption spectroscopy (IRRAS) in an electrochemical environment. We demonstrated the potential of the combined experiment by correlating the structural changes to the adsorption behavior of a Pt(111) single crystal electrode during CO and surface oxidation. In particular, we were able to distinguish between the adsorbate-induced restructuring and electrochemical oxidation of the Pt(111) surface under potential control. The experimental setup is compatible with all types of planar model electrodes, such as single crystals, supported nanoparticles on planar electrodes, and nanostructured films. As a unique feature of the approach, potential-dependent chemical and structural information can be obtained in a single experiment. The chemical information available from IRRAS includes the nature of adsorbates, intermediates, poisons, or promoters and their adsorption sites and geometry at the electrode and in solution (using polarization-dependent data). The structural information available from HE-SXRD includes lattice parameters, surface relaxations and roughness, nanoparticle size, shape, orientation, and information on segregation, dealloying, or phase transformations. By recording the data in a simultaneous fashion, correlations between structure and reactivity can be obtained in a much more reliable and reproducible fashion. Finally, we note that the here described instrument is compatible with different beamlines at DESY and the European Synchrotron Radiation Facility (ESRF) and is part of the DESY infrastructure which is available to users via the common application procedures.[62]

Experimental Section. The experiment was performed at the Physics Hutch at beamline P07 of Petra III, DESY.[48] The glassware and the electrochemical cell parts were soaked overnight in 1 g L^{-1} $KMnO_4$/0.5 M H_2SO_4 solution, followed by boiling in ultrapure water (18.2 MΩ·cm, Elga purelab flex) 4 to 5 times. The electrochemical cell was assembled with a CaF_2 hemisphere at the bottom, which serves as the IR transparent window, and has a diameter of 2.5 cm. The Pt(111) sample (MaTeck) was annealed for 2 min in a butane flame and cooled in a H_2/Ar atmosphere (ratio ∼3:1). After the single crystal cooled to room temperature, the surface of the Pt sample was protected by a drop of ultrapure water and transferred to the electrochemical cell. The electrolyte, 0.1 M $HClO_4$, was prepared using perchloric acid (99.999% trace metal basis, Sigma-Aldrich). A potentiostat (Gamry Reference 600+) was used to control the potentials in a three-electrode configuration. A miniaturized reversible hydrogen electrode (RHE, HydroFlex) and a Pt wire were used as RE and CE, respectively. Electrochemical IR spectra were acquired with a FTIR spectrometer with evacuated beampath (Bruker Vertex 80v) and an external IR chamber purged with nitrogen (see main text for details). Before the experiment, the external IR chamber was purged with N_2 for at least 1 h, and the flow was kept through the experiment. IR spectra were acquired with a liquid-nitrogen-cooled mercury cadmium telluride (MCT) narrow band detector. HE-SXRD was measured with an X-ray incidence angle of 0.05°, which is slightly above the critical angle of total external reflection for Pt at the used photon energy of 73.94 keV. HE-SXRD data were recorded using a 2D area detector (Varex XRD4343RF) with a total sensitive area of 432 × 432 mm^2 and a pixel size of 150 × 150 μm^2. This detector was placed at a distance of 1400 mm from the sample. The high-intensity Bragg peaks from both the Pt sample and the CaF_2 IR window were blocked using lead absorber pieces. A hexagonal surface unit cell ($a = b = 2.77$ Å, $c = 6.80$ Å) was chosen such that the a^* and b^* reciprocal space vectors describe the surface plane while the c^* vector lies along the surface normal. The corresponding H, K, and L coordinates were defined using a Pt lattice constant of 3.924 Å. Data processing,[63] i.e., background subtraction, intensity correction, and signal integration, was performed using home-written scripts in Wavemetrics Igor Pro. The ANAROD package was used to fit a structural model to the data.[64]

■ ASSOCIATED CONTENT

Data Availability Statement

The data that support the findings of this study are presented in the Letter and the Supporting Information. Source data are provided at Zenodo: DOI 10.5281/zenodo.8327394.

Supporting Information

The Supporting Information is available free of charge at https://pubs.acs.org/doi/10.1021/acs.jpclett.3c01777.

Determination of the Stark slope in the IRRAS data; diffusion of CO from the bulk solution into the thin layer; parameters used to fit the HE-SXRD data; simulated CTRs in the presence and absence of a CO adlayer; illustration of the place-exchange mechanism (PDF)

■ AUTHOR INFORMATION

Corresponding Author

Olaf Brummel − *Interface Research and Catalysis, ECRC, Friedrich-Alexander-Universität Erlangen-Nürnberg, 91058 Erlangen, Germany;* orcid.org/0000-0001-5968-0774; Email: olaf.brummel@fau.de

Authors

Leon Jacobse − *Centre for X-ray and Nano Science CXNS, Deutsches Elektronen-Synchrotron DESY, 22607 Hamburg, Germany;* orcid.org/0000-0002-2825-0963

Alexander Simanenko − *Interface Research and Catalysis, ECRC, Friedrich-Alexander-Universität Erlangen-Nürnberg, 91058 Erlangen, Germany*

Xin Deng − *Interface Research and Catalysis, ECRC, Friedrich-Alexander-Universität Erlangen-Nürnberg, 91058 Erlangen, Germany; Centre for X-ray and Nano Science CXNS, Deutsches Elektronen-Synchrotron DESY, 22607 Hamburg, Germany*

Simon Geile − *Centre for X-ray and Nano Science CXNS, Deutsches Elektronen-Synchrotron DESY, 22607 Hamburg, Germany*

Olof Gutowski − *Deutsches Elektronen-Synchrotron DESY, 22607 Hamburg, Germany;* orcid.org/0000-0001-5514-4480

Vedran Vonk − *Centre for X-ray and Nano Science CXNS, Deutsches Elektronen-Synchrotron DESY, 22607 Hamburg, Germany;* orcid.org/0000-0001-9854-1101

Yaroslava Lykhach − *Interface Research and Catalysis, ECRC, Friedrich-Alexander-Universität Erlangen-Nürnberg, 91058 Erlangen, Germany;* orcid.org/0000-0003-3989-0365

Andreas Stierle − *Centre for X-ray and Nano Science CXNS, Deutsches Elektronen-Synchrotron DESY, 22607 Hamburg,*

Germany; Fachbereich Physik, Universität Hamburg, 20355 Hamburg, Germany; orcid.org/0000-0002-0303-6282

Jörg Libuda − *Interface Research and Catalysis, ECRC, Friedrich-Alexander-Universität Erlangen-Nürnberg, 91058 Erlangen, Germany;* orcid.org/0000-0003-4713-5941

Complete contact information is available at: https://pubs.acs.org/10.1021/acs.jpclett.3c01777

Notes

The authors declare no competing financial interest.

■ ACKNOWLEDGMENTS

The authors acknowledge financial support by the German Federal ministry of Education and Research (BMBF, Project Combined Infrared and X-ray Analytics of Energy Materials, CIXenergy 05K19WE1). We acknowledge DESY (Hamburg, Germany), a member of the Helmholtz Association HGF, for the provision of experimental facilities. Parts of this research were performed at PETRA III and DESY NanoLab, and we thank Ann-Christin Dippel for organizing and coordinating the beamtime at beamline P07 and Monika Dahdouli and Milena Lippmann for assistance in using the chemical laboratory. Beamtime was allocated for proposal I-20211206. The research leading to this result has been supported by the project CALIPSOplus under the Grant Agreement 730872 from the EU Framework Programme for Research and Innovation HORIZON 2020. The authors acknowledge additional support by the Deutsche Forschungsgemeinschaft (DFG) within the Collaborative Research Centre SFB 1452−Catalysis at Liquid Interfaces, Research Unit FOR 5499 "Molecular Solar Energy Management−Chemistry of MOST Systems" (project 496207555), further projects (322419553, 431733372, 453560721), and the Bavarian ministry of Economic Affairs, Regional Development and Energy.

■ REFERENCES

(1) Cui, C.; Gan, L.; Heggen, M.; Rudi, S.; Strasser, P. Compositional Segregation in Shaped Pt Alloy Nanoparticles and their Structural Behaviour during Electrocatalysis. *Nat. Mater.* **2013**, *12* (8), 765−771.

(2) Birdja, Y. Y.; Pérez-Gallent, E.; Figueiredo, M. C.; Göttle, A. J.; Calle-Vallejo, F.; Koper, M. T. M. Advances and challenges in understanding the electrocatalytic conversion of carbon dioxide to fuels. *Nature Energy* **2019**, *4* (9), 732−745.

(3) Ledezma-Yanez, I.; Wallace, W. D. Z.; Sebastián-Pascual, P.; Climent, V.; Feliu, J. M.; Koper, M. T. M. Interfacial water reorganization as a pH-dependent descriptor of the hydrogen evolution rate on platinum electrodes. *Nature Energy* **2017**, *2* (4), 17031.

(4) Gao, D.; Arán-Ais, R. M.; Jeon, H. S.; Roldan Cuenya, B. Rational catalyst and electrolyte design for CO_2 electroreduction towards multicarbon products. *Nature Catalysis* **2019**, *2* (3), 198−210.

(5) Timoshenko, J.; Bergmann, A.; Rettenmaier, C.; Herzog, A.; Arán-Ais, R. M.; Jeon, H. S.; Haase, F. T.; Hejral, U.; Grosse, P.; Kühl, S.; Davis, E. M.; Tian, J.; Magnussen, O.; Roldan Cuenya, B. Steering the structure and selectivity of CO_2 electroreduction catalysts by potential pulses. *Nature Catalysis* **2022**, *5* (4), 259−267.

(6) Magnussen, O. M.; Groß, A. Toward an Atomic-Scale Understanding of Electrochemical Interface Structure and Dynamics. *J. Am. Chem. Soc.* **2019**, *141* (12), 4777−4790.

(7) Katsounaros, I.; Cherevko, S.; Zeradjanin, A. R.; Mayrhofer, K. J. J. Oxygen Electrochemistry as a Cornerstone for Sustainable Energy Conversion. *Angew. Chem., Int. Ed.* **2014**, *53* (1), 102−121.

(8) Seh, Z. W.; Kibsgaard, J.; Dickens, C. F.; Chorkendorff, I.; Nørskov, J. K.; Jaramillo, T. F. Combining Theory and Experiment in Electrocatalysis: Insights into Materials Design. *Science* **2017**, *355* (6321), No. eaad4998.

(9) Mistry, H.; Varela, A. S.; Kühl, S.; Strasser, P.; Cuenya, B. R. Nanostructured Electrocatalysts with Tunable Activity and Selectivity. *Nat. Rev. Mater.* **2016**, *1*, 16009.

(10) Bandarenka, A. S.; Ventosa, E.; Maljusch, A.; Masa, J.; Schuhmann, W. Techniques and methodologies in modern electrocatalysis: evaluation of activity, selectivity and stability of catalytic materials. *Analyst* **2014**, *139* (6), 1274−1291.

(11) Chen, J.; Wang, L. Effects of the Catalyst Dynamic Changes and Influence of the Reaction Environment on the Performance of Electrochemical CO_2 Reduction. *Adv. Mater.* **2022**, *34* (25), 2103900.

(12) Yuan, Y.; Wang, Q.; Qiao, Y.; Chen, X.; Yang, Z.; Lai, W.; Chen, T.; Zhang, G.; Duan, H.; Liu, M.; Huang, H. In Situ Structural Reconstruction to Generate the Active Sites for CO_2 Electroreduction on Bismuth Ultrathin Nanosheets. *Adv. Energy Mater.* **2022**, *12* (29), 2200970.

(13) Kleijn, S. E. F.; Lai, S. C. S.; Koper, M. T. M.; Unwin, P. R. Electrochemistry of Nanoparticles. *Angew. Chem., Int. Ed.* **2014**, *53* (14), 3558−3586.

(14) Mayrhofer, K. J. J.; Meier, J. C.; Ashton, S. J.; Wiberg, G. K. H.; Kraus, F.; Hanzlik, M.; Arenz, M. Fuel cell catalyst degradation on the nanoscale. *Electrochem. Commun.* **2008**, *10* (8), 1144−1147.

(15) Stumm, C.; Bertram, M.; Kastenmeier, M.; Speck, F. D.; Sun, Z.; Rodríguez-Fernández, J.; Lauritsen, J. V.; Mayrhofer, K. J. J.; Cherevko, S.; Brummel, O.; Libuda, J. Structural Dynamics of Ultrathin Cobalt Oxide Nanoislands under Potential Control. *Adv. Funct. Mater.* **2021**, *31*, 2009923.

(16) Mom, R. V.; Falling, L. J.; Kasian, O.; Algara-Siller, G.; Teschner, D.; Crabtree, R. H.; Knop-Gericke, A.; Mayrhofer, K. J. J.; Velasco-Vélez, J.-J.; Jones, T. E. Operando Structure-Activity-Stability Relationship of Iridium Oxides during the Oxygen Evolution Reaction. *ACS Catal.* **2022**, *12* (9), 5174−5184.

(17) Zhu, Y.; Chen, H.-C.; Hsu, C.-S.; Lin, T.-S.; Chang, C.-J.; Chang, S.-C.; Tsai, L.-D.; Chen, H. M. Operando Unraveling of the Structural and Chemical Stability of P-Substituted $CoSe_2$ Electrocatalysts toward Hydrogen and Oxygen Evolution Reactions in Alkaline Electrolyte. *ACS Energy Lett.* **2019**, *4* (4), 987−994.

(18) Sakong, S.; Groß, A. Methanol Oxidation on Pt(111) from First-Principles in Heterogeneous and Electrocatalysis. *Electrocatalysis* **2017**, *8* (6), 577−586.

(19) Yang, T.; Yang, J.; Deng, X.; Franz, E.; Fromm, L.; Taccardi, N.; Liu, Z.; Görling, A.; Wasserscheid, P.; Brummel, O.; Libuda, J. Modifying the Electrocatalytic Selectivity of Oxidation Reactions with Ionic Liquids. *Angew. Chem., Int. Ed.* **2022**, *61* (29), No. e202202957.

(20) Samant, M. G.; Toney, M. F.; Borges, G. L.; Blum, L.; Melroy, O. R. Grazing incidence x-ray diffraction of lead monolayers at a silver (111) and gold (111) electrode/electrolyte interface. *J. Phys. Chem.* **1988**, *92* (1), 220−225.

(21) Sonnenfeld, R.; Hansma, P. K. Atomic-Resolution Microscopy in Water. *Science* **1986**, *232* (4747), 211−213.

(22) Lustenberger, P.; Rohrer, H.; Christoph, R.; Siegenthaler, H. Scanning Tunneling Microscopy at Potential Controlled Electrode Surfaces in Electrolytic Environment. *J. Electroanal. Chem. Interfacial Electrochem.* **1988**, *243* (1), 225−235.

(23) Wiechers, J.; Twomey, T.; Kolb, D. M.; Behm, R. J. An In-Situ Scanning Tunneling Microscopy Study of Au(111) with Atomic Scale Resolution. *J. Electroanal. Chem. Interfacial Electrochem.* **1988**, *248* (2), 451−460.

(24) Manne, S.; Hansma, P. K.; Massie, J.; Elings, V. B.; Gewirth, A. A. Atomic-Resolution Electrochemistry with the Atomic Force Microscope: Copper Deposition on Gold. *Science* **1991**, *251* (4990), 183−186.

(25) de Jonge, N.; Ross, F. M. Electron microscopy of specimens in liquid. *Nat. Nanotechnol.* **2011**, *6* (11), 695−704.

(26) Ross, F. M. Opportunities and challenges in liquid cell electron microscopy. *Science* **2015**, *350* (6267), aaa9886.

(27) Hodnik, N.; Dehm, G.; Mayrhofer, K. J. J. Importance and Challenges of Electrochemical in Situ Liquid Cell Electron Microscopy for Energy Conversion Research. *Acc. Chem. Res.* **2016**, *49* (9), 2015−2022.
(28) Bewick, A.; Kunimatsu, K. Infra red spectroscopy of the electrode-electrolyte interphase. *Surf. Sci.* **1980**, *101* (1), 131−138.
(29) Bewick, A.; Kunimatsu, K.; Stanley Pons, B. Infra red spectroscopy of the electrode-electrolyte interphase. *Electrochim. Acta* **1980**, *25* (4), 465−468.
(30) Bewick, A.; Kunimatsu, K.; Pons, B. S.; Russell, J. W. Electrochemically modulated infrared spectroscopy (EMIRS): Experimental details. *Journal of Electroanalytical Chemistry and Interfacial Electrochemistry* **1984**, *160* (1), 47−61.
(31) Osawa, M. Dynamic processes in electrochemical reactions studied by surface-enhanced infrared absorption spectroscopy (SEIRAS). *Bull. Chem. Soc. Jpn.* **1997**, *70* (12), 2861−2880.
(32) Iwasita, T.; Nart, F. C. In situ infrared spectroscopy at electrochemical interfaces. *Prog. Surf. Sci.* **1997**, *55* (4), 271−340.
(33) Tadjeddine, A.; Le Rille, A. *Sum and Difference Frequency Generation at Electrode Surfaces*; Dekker: New York, 1999.
(34) Axnanda, S.; Crumlin, E. J.; Mao, B.; Rani, S.; Chang, R.; Karlsson, P. G.; Edwards, M. O. M.; Lundqvist, M.; Moberg, R.; Ross, P.; Hussain, Z.; Liu, Z. Using "Tender" X-ray Ambient Pressure X-Ray Photoelectron Spectroscopy as A Direct Probe of Solid-Liquid Interface. *Sci. Rep.* **2015**, *5*, 9788.
(35) Brummel, O.; Lykhach, Y.; Ralaiarisoa, M.; Berasategui, M.; Kastenmeier, M.; Fusek, L.; Simanenko, A.; Gu, W.; Clark, P. C. J.; Yivlialin, R.; Sear, M. J.; Mysliveček, J.; Favaro, M.; Starr, D.; Libuda, J. A Versatile Approach to Electrochemical *In Situ* Ambient-Pressure X-ray Photoelectron Spectroscopy: Application to a Complex Model Catalyst. *J. Phys. Chem. Lett.* **2022**, *13* (47), 11015−11022.
(36) Timoshenko, J.; Roldan Cuenya, B. In Situ/Operando Electrocatalyst Characterization by X-ray Absorption Spectroscopy. *Chem. Rev.* **2021**, *121* (2), 882−961.
(37) Villegas, I.; Weaver, M. J. Carbon Monoxide Adlayer Structures on Platinum (111) Electrodes: A Synergy between In-Situ Scanning Tunneling Microscopy and Infrared Spectroscopy. *J. Chem. Phys.* **1994**, *101* (2), 1648−1660.
(38) Marković, N. M.; Lucas, C. A.; Rodes, A.; Stamenković, V.; Ross, P. N. Surface electrochemistry of CO on Pt(111): anion effects. *Surf. Sci.* **2002**, *499* (2), L149−L158.
(39) Newton, M. A.; van Beek, W. Combining synchrotron-based X-ray techniques with vibrational spectroscopies for the in situ study of heterogeneous catalysts: a view from a bridge. *Chem. Soc. Rev.* **2010**, *39* (12), 4845−4863.
(40) Hinokuma, S.; Wiker, G.; Suganuma, T.; Bansode, A.; Stoian, D.; Huertas, S. C.; Molina, S.; Shafir, A.; Rønning, M.; van Beek, W.; Urakawa, A. Versatile IR Spectroscopy Combined with Synchrotron XAS-XRD: Chemical, Electronic, and Structural Insights during Thermal Treatment of MOF Materials. *Eur. J. Inorg. Chem.* **2018**, *2018* (17), 1847−1853.
(41) Marcelli, A.; Innocenzi, P.; Malfatti, L.; Newton, M. A.; Rau, J. V.; Ritter, E.; Schade, U.; Xu, W. IR and X-ray time-resolved simultaneous experiments: an opportunity to investigate the dynamics of complex systems and non-equilibrium phenomena using third-generation synchrotron radiation sources. *Journal of Synchrotron Radiation* **2012**, *19* (6), 892−904.
(42) Pfaff, S.; Zhou, J.; Hejral, U.; Gustafson, J.; Shipilin, M.; Albertin, S.; Blomberg, S.; Gutowski, O.; Dippel, A.; Lundgren, E.; Zetterberg, J. Combining high-energy X-ray diffraction with Surface Optical Reflectance and Planar Laser Induced Fluorescence for operando catalyst surface characterization. *Rev. Sci. Instrum.* **2019**, *90* (3), 033703.
(43) Rämisch, L.; Gericke, S. M.; Pfaff, S.; Lundgren, E.; Zetterberg, J. Infrared surface spectroscopy and surface optical reflectance for operando catalyst surface characterization. *Appl. Surf. Sci.* **2022**, *578*, 152048.
(44) Newton, M. A.; Di Michiel, M.; Kubacka, A.; Fernández-García, M. Combining Time-Resolved Hard X-ray Diffraction and Diffuse Reflectance Infrared Spectroscopy To Illuminate CO Dissociation and Transient Carbon Storage by Supported Pd Nanoparticles during CO/NO Cycling. *J. Am. Chem. Soc.* **2010**, *132* (13), 4540−4541.
(45) Hejral, U.; Shipilin, M.; Gustafson, J.; Stierle, A.; Lundgren, E. High energy surface x-ray diffraction applied to model catalyst surfaces at work. *J. Phys.: Condens. Matter* **2021**, *33* (7), 073001.
(46) Hubbell, J. H.; Seltzer, S. M. *X-Ray Mass Attenuation Coefficients*; National Institute of Standards and Technology (NIST): 2004.
(47) Hejral, U.; Müller, P.; Shipilin, M.; Gustafson, J.; Franz, D.; Shayduk, R.; Rütt, U.; Zhang, C.; Merte, L. R.; Lundgren, E.; Vonk, V.; Stierle, A. High-Energy X-Ray Dffraction from Surfaces and Nanoparticles. *Phys. Rev. B* **2017**, *96* (19), 195433.
(48) Schell, N.; King, A.; Beckmann, F.; Fischer, T.; Müller, M.; Schreyer, A. The High Energy Materials Science Beamline (HEMS) at PETRA III. *Mater. Sci. Forum* **2013**, *772*, 57−61.
(49) García, G.; Koper, M. T. M. Carbon Monoxide Oxidation on Pt Single Crystal Electrodes: Understanding the Catalysis for Low Temperature Fuel Cells. *ChemPhysChem* **2011**, *12* (11), 2064−2072.
(50) Wei, J.; Amirbeigiarab, R.; Chen, Y.-X.; Sakong, S.; Gross, A.; Magnussen, O. M. The Dynamic Nature of CO Adlayers on Pt(111) Electrodes. *Angew. Chem., Int. Ed.* **2020**, *59* (15), 6182−6186.
(51) Wei, J.; Chen, Y.-X.; Magnussen, O. M. Electrochemical In Situ Video-STM Studies of the Phase Transition of CO Adlayers on Pt(111) Electrodes. *J. Phys. Chem. C* **2021**, *125* (5), 3066−3072.
(52) Brummel, O.; Waidhas, F.; Faisal, F.; Fiala, R.; Vorokhta, M.; Khalakhan, I.; Dubau, M.; Figueroba, A.; Kovács, G.; Aleksandrov, H. A.; Vayssilov, G. N.; Kozlov, S. M.; Neyman, K. M.; Matolín, V.; Libuda, J. Stabilization of Small Platinum Nanoparticles on Pt-CeO_2 Thin Film Electrocatalysts During Methanol Oxidation. *J. Phys. Chem. C* **2016**, *120* (35), 19723−19736.
(53) Jacobse, L.; Schuster, R.; Pfrommer, J.; Deng, X.; Dolling, S.; Weber, T.; Gutowski, O.; Dippel, A.-C.; Brummel, O.; Lykhach, Y.; Over, H.; Libuda, J.; Vonk, V.; Stierle, A. A Combined Rotating Disk Electrode-Surface X-Ray Diffraction Setup for Surface Structure Characterization in Electrocatalysis. *Rev. Sci. Instrum.* **2022**, *93* (6), 065111.
(54) You, H.; Zurawski, D. J.; Nagy, Z.; Yonco, R. M. In-situ x-ray reflectivity study of incipient oxidation of Pt(111) surface in electrolyte solutions. *J. Chem. Phys.* **1994**, *100* (6), 4699−4702.
(55) Tidswell, I. M.; Markovic, N. M.; Ross, P. N. Potential dependent surface structure of the Pt(1 1 1) electrolyte interface. *J. Electroanal. Chem.* **1994**, *376* (1), 119−126.
(56) Liu, Y.; Barbour, A.; Komanicky, V.; You, H. X-ray Crystal Truncation Rod Studies of Surface Oxidation and Reduction on Pt(111). *J. Phys. Chem. C* **2016**, *120* (29), 16174−16178.
(57) Ruge, M.; Drnec, J.; Rahn, B.; Reikowski, F.; Harrington, D. A.; Carlà, F.; Felici, R.; Stettner, J.; Magnussen, O. M. Electrochemical Oxidation of Smooth and Nanoscale Rough Pt(111): An In Situ Surface X-ray Scattering Study. *J. Electrochem. Soc.* **2017**, *164* (9), H608.
(58) Jacobse, L.; Vonk, V.; McCrum, I. T.; Seitz, C.; Koper, M. T. M.; Rost, M. J.; Stierle, A. Electrochemical oxidation of Pt(111) beyond the place-exchange model. *Electrochim. Acta* **2022**, *407*, 139881.
(59) Leon, J.; Robert, H. *Electrochemical oxidation of Pt(111) beyond the Place-Exchange Model*; Cassyni: 2023.
(60) Sandbeck, D. J. S.; Brummel, O.; Mayrhofer, K. J. J.; Libuda, J.; Katsounaros, I.; Cherevko, S. Dissolution of Platinum Single Crystals in Acidic Medium. *ChemPhysChem* **2019**, *20* (22), 2997−3003.
(61) Lucas, C. A.; Marković, N. M.; Ross, P. N. The adsorption and oxidation of carbon monoxide at the Pt(111)/electrolyte interface: atomic structure and surface relaxation. *Surf. Sci.* **1999**, *425* (1), L381−L386.
(62) Noei, H.; Vonk, V.; Keller, T.; Röhlsberger, R.; Stierle, A. DESY NanoLab, Deutsches Elektronen Synchrotron (DESY). *J. Large-Scale Res. Facil* **2016**, *2*, A76.
(63) Shipilin, M.; Hejral, U.; Lundgren, E.; Merte, L. R.; Zhang, C.; Stierle, A.; Ruett, U.; Gutowski, O.; Skoglundh, M.; Carlsson, P.-A.;

https://doi.org/10.1021/acs.jpclett.3c01777
J. Phys. Chem. Lett. XXXX, XXX, XXX−XXX

682 Gustafson, J. Quantitative surface structure determination using in
683 situ high-energy SXRD: Surface oxide formation on Pd(100) during
684 catalytic CO oxidation. *Surf. Sci.* **2014**, *630*, 229−235.
685 (64) Vlieg, E. ROD: a program for surface X-ray crystallography. *J.*
686 *Appl. Crystallogr.* **2000**, *33* (2), 401−405.

https://doi.org/10.1021/acs.jpclett.3c01777
J. Phys. Chem. Lett. XXXX, XXX, XXX−XXX